energies

Article

A Novel Analytical Equivalent Circuit for Single-Sided Linear Induction Motors Considering Secondary Leakage Reactance

Daniel R. Gomes [1,2] and Ivan E. Chabu [1,*]

[1] Department of Energy and Automation, Polytechnic School of University of São Paulo,
São Paulo 05508-010, Brazil
[2] Mauá Institute of Technology, São Caetano do Sul 09580-900, Brazil
* Correspondence: ichabu@pea.usp.br

Abstract: Single-sided linear induction motors usually appear in magnetic levitation systems of transportation. Since the beginning of such developments, edge effects represent one of the great challenges to overcome in analytical modelling. For almost four decades, in order to simplify the mathematical treatment of border effects, most analytical models have not considered the secondary leakage flux properly. Although concise and accurate in most cases, such approaches have deficiencies in slotted secondaries. This paper presents an analytical equivalent circuit that considers the secondary reactance for both edge effects, i.e., entry and exit sides. The proposed approach uses an analogical RLC circuit which describes the behavior of magnetizing (exit) and demagnetizing (entry) waves, as well as adapted correction factors for transverse effects. By means of an 8 pole/120–175 N prototype, the measured thrust and vertical forces remarkably validate the model for frequencies equal or higher than 60 Hz. The relevance of secondary reactance in such cases can be explained by accounting its influence, specially, in the rise of the demagnetizing entry wave.

Keywords: equivalent circuit; single-sided linear induction motor; slotted secondary leakage flux; longitudinal end effects

check for updates

Citation: Gomes, D.R.; Chabu, I.E. A Novel Analytical Equivalent Circuit for Single-Sided Linear Induction Motors Considering Secondary Leakage Reactance. *Energies* **2023**, *16*, 1261. https://doi.org/10.3390/en16031261

Academic Editors: Andrea Tortella and Mauro Andriollo

Received: 14 December 2022
Revised: 6 January 2023
Accepted: 19 January 2023
Published: 24 January 2023

1. Introduction and Literature Review

Linear induction motors (LIM) has been object of study for over a hundred years [1], having its applications mainly in machine tools and transportation. The single-sided linear induction motor, a particular case of LIM, appear specially in magnetic levitation systems [2].

Since the well-known publication on LIM's [3], intense research has followed on normal and traction forces in this type of machine [4]. The external characteristic of the linear induction motor strongly depends on the behavior of the electromagnetic travelling wave in its air gap, which has also moved scientific research to focus efforts on the so-called edge effects, resulting from the inevitable open magnetic circuit of that configuration [5].

Later, the University of Tokyo advanced in the modeling of linear induction motors with double primary, focusing on equating the edge effects [6]. The focus was not to develop a representative circuit, but to propose more accurate expressions for pulling force, output power, line current, efficiency and power factor, taking into account edge effects. In addition, the aforementioned work proposed a compensating winding located at the entry edge, with the aim of mitigating the undesirable effects, specially in the cases of high-speed applications, where such effects increase appreciably.

Until then, the approaches were established in a two-dimensional way. In the late 1970s, quasi-three-dimensional mathematical models began to be used (a two-dimensional analysis with compensating corrections for the third dimension). The work carried out with such a treatment focused on a linear motor with double primary and massive secondary [7], but also applicable to cases of single primary, considering a solid secondary with an magnetic yoke (back iron). The transverse and longitudinal edge effects were considered by applying Ampère's Circuit Law in two directions, as well as the effects resulting from the stepped winding, that is, with partially filled slots at the borders of the primary, considering two displaced current blades. A simple equivalent circuit was presented, but only for consideration of the secondary power and induced voltages (in this case considered balanced, even recognizing the unbalance resulting from longitudinal edge effects).

At the same time, equivalent circuit models sought to incorporate the effects of open magnetic circuits through correction factors [8,9]. Since then, some advances were made in dynamic parameter models [10], optimization of the primary winding aiming a better traction performance [11] and equivalent circuits, including effects of partially filled primary slots [12].

One of the most important publications for the present paper made a direct analogy with the equivalent circuit of the rotary induction motor [13]. The focus was on corrections factors, resulting from edge effects in relation to the magnetizing branch. The cited paper had considerable weight in later publications and is still used today.

However, all the works cited addressed the issue considering a secondary without slots, either formed entirely of non-ferrous material or made of non-ferrous sheet, generally aluminum, with a back iron. Few publications considered a slotted secondary in the investigation, some in the analysis of normal and thrust forces in the aforementioned configuration [14] and others in the relevance of the contact resistance existing in the welded cage [15]. Particularly, in a publication on design optimization considering a slotted secondary, eventually called just a "ladder", considered a circuit for massive secondaries [16]. See Figure 1 for different secondaries concepts.

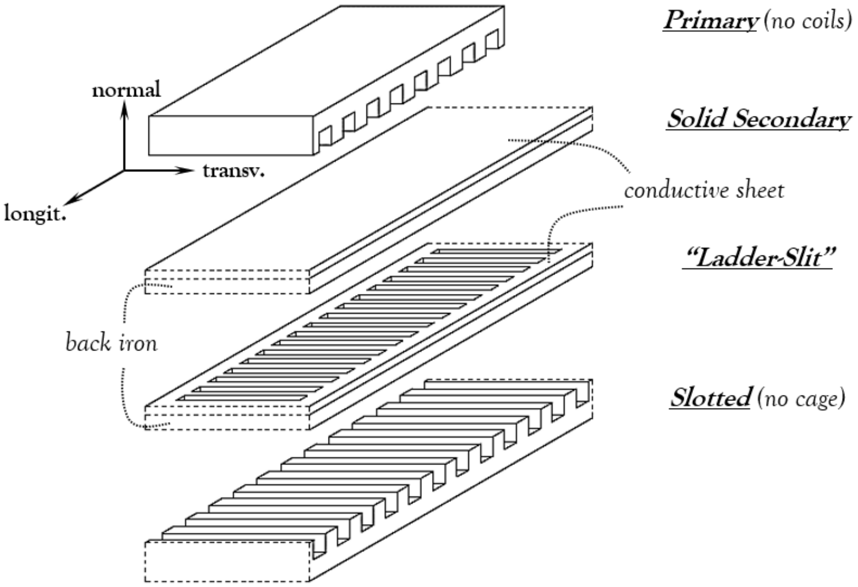

Figure 1. Difference between solid, ladder, and slotted secondaries.

Throughout the present work, the expression "slotted secondary" will refer to the traditional slotted structure in the form of a cage, and not to the secondary called "ladder-slit", which consists of a grooved conductive plate, which gained attention from the 1990s onwards [17,18]. With a grooved aluminum plate, it was noticed that there was an increase in the resulting tensile strength and a decrease in material cost. Recently, some attention has been given to optimization in the design of such a configuration [19].

Other more recent efforts [20,21] focused their attention on solid sheet type secondaries, eventually with lateral asymmetry in the secondary [22], proposing tests to obtain parameters [23] or an equivalent circuit for solid secondary width optimization. Yet some works have used the conventional Duncan's approach with modifications, aiming design refinements [24–28]. Some of the advances obtained in the above mentioned works were considered here. Once again, however, it should be noted that such publications did not consider the effect of secondary leakage, when similar in magnitude to that of the primary, on the demagnetizing and magnetizing waves at the entry and exit edges, respectively.

As far as we are aware, there is no equivalent circuit proposal that considers the secondary leakage effect on both edge effects (entry and exit). A fine job has been initiated in [12], but it did not consider the exit-magnetizing component or the vertical forces. Without intending to completely fill the gap, the present work proposes to be a support to the designer that, having at hand the pre-construction data of the linear motor, could determine the parameters of the equivalent circuit and, with basic computational resources, reach satisfactory results regarding the performance of traction and vertical forces. In addition, one would be able to compare such external characteristics, among others, in relation to the secondary configuration alternatives.

Taking into account that the slotted configuration appears in the prominent MAGLEV COBRA project of the Federal University of Rio de Janeiro [29,30], such an advance in modelling is considered relevant.

Finally, it is also intended to establish a experimental validation of the new analytical model for slotted secondaries, by means of a prototype specially manufactured, where thrust and vertical forces can be measured. It will be seen, as well, that the proposed model can be useful even in solid secondaries, be the continuous or the ladder-slit one, when the frequency is high enough.

2. New Equivalent Circuit

In this section, the objective is to highlight the contribution of the present work. In comparison with the most present analytical model in the literature [13], the proposed one adds the effect of secondary flux dispersion, once neglected. In this way, the demagnetizing wave at the entry border will have its shape affected. In addition to that, the magnetizing wave at the exit border will be accounted for in the circuit, which was not the case before.

In solid (continuous or "ladder-slit") secondaries, the secondary leakage flux is, in fact, substantially lower than the primary. In slotted secondaries, however, such values become similar. Therefore, the proposed model will have greater weight in the latter cases.

According to [13], the main difference between rotating and linear induction motors is that, in the latter, as the primary moves, the secondary continuously presents "new" conductive material at the entry edge, which will oppose the sudden increase in magnetic flux. Similarly, at the exit border, there will be an opposition in the secondary to the sudden decrease in flux. Such phenomena mainly affect the flux distribution in the air gap, which would justify a model with correction factors in the magnetizing branch, according to the source cited. It is worth mentioning that such considerations do not concern the secondary load component.

2.1. Longitudinal Edge Effects

Longitudinal edge effects at entry and exit borders depend on time constants involving secondary and magnetization inductances and secondary ohmic resistance. Such time constants define rise and fall times of the armature reaction at the edges. The spatial distribution of flux along the air gap will also depend on the displacement speed.

At time zero, the secondary reaction current at the entry edge, referred to the primary circuit, will tend to cancel out the primary magnetizing current, almost equaling it in magnitude. Its increase will be quick, since at the input interface the only inductance to delay it will be that of secondary leakage, since the primary and secondary circuits of the new material are not yet linked.

Then, the decay of the demagnetizing wave will no longer be so fast, since now the time constant contemplates mutual flux between the parts, in addition to the secondary leakage.

Figure 2 illustrates the behavior of the secondary magnetomotive force in this demagnetizing effect at a constant speed, also considering the slots fully filled at the ends.

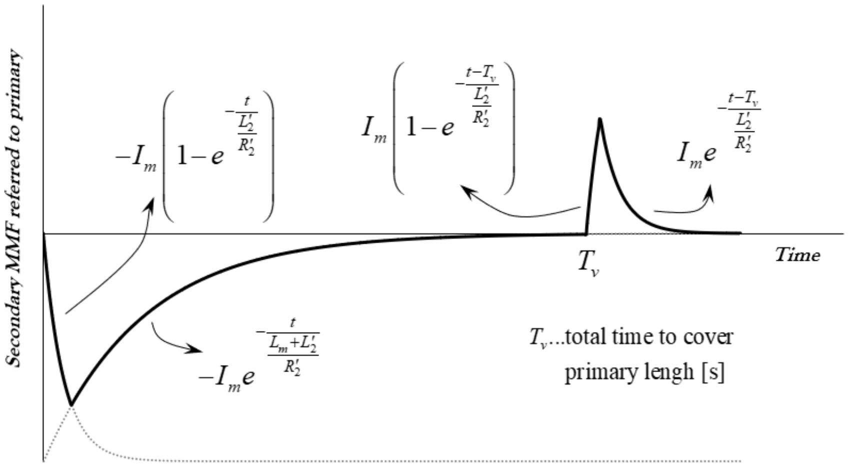

Figure 2. Secondary mmf reaction behavior through time.

At the right hand of Figure 2, one can see also the magnetizing component of secondary reaction, which takes place at the exit border.

In solid secondaries, the leakage inductance is very low, and the areas described by the time constant exponentials $L'_2/R'_2 = T_{2\ell}$ are neglected without significant loss of precision, leaving only the time constant component $(L'_2 + L_m)/R'_2 = T_2$ as significant. According to [13], although the value of the secondary reaction varies along the length of the motor, its reflection to the primary winding can be considered as an average current in phase opposition to the magnetization current. Neglecting the secondary leakage reactance will lead to the circuit of Figure 3. In addition to the demagnetizing effect, there will be an increase in parasitic losses due to the path taken by the secondary reaction currents. Please see [13] for more details.

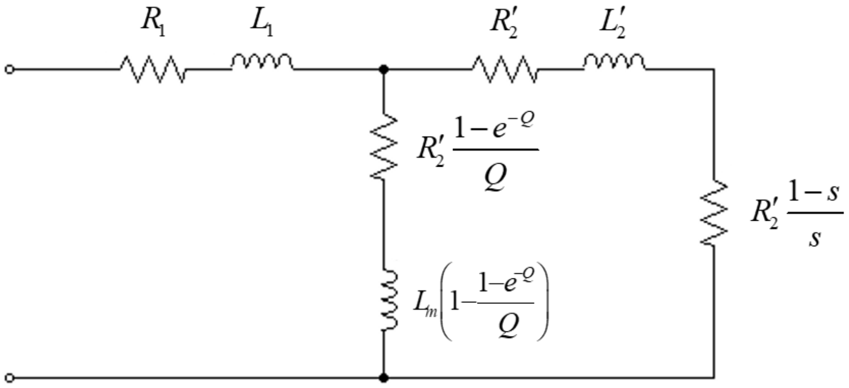

Figure 3. Resulting equivalent circuit according to [13].

In the slotted secondary, leakage inductance is significantly higher than in solid and ladder-slit models. The rise of the demagnetizing secondary component current that reacts to the magnetization at the input edge, as it depends on the secondary dispersion, should now be included in the calculation. Additionally, the magnetizing component that opposes demagnetization at the exit edge must be considered.

The edges of entry and exit waves shown in Figure 2 obviously do not correspond to reality, given their discontinuities. Rounded edges are more coherent—see Figure 4. Therefore, to analytically describe the behavior of the waves, the authors propose an analogous (not equivalent!) RLC circuit—Figure 5, whose transient response will correspond to the demagnetizing and magnetizing waves. In the case of [13], $L'_2 \approx 0$ for the purposes above mentioned, even though for losses and vertical forces there is partial consideration. See below that the analogous capacitances are functions of the resistances and inductances.

See the secondary leakage influence comparison at Figure 4. It is easy to see that, as the secondary dispersion increases, the effect of the demagnetizing longitudinal edge may be greater. On the other hand, the magnetizing component at the leading edge is no longer negligible.

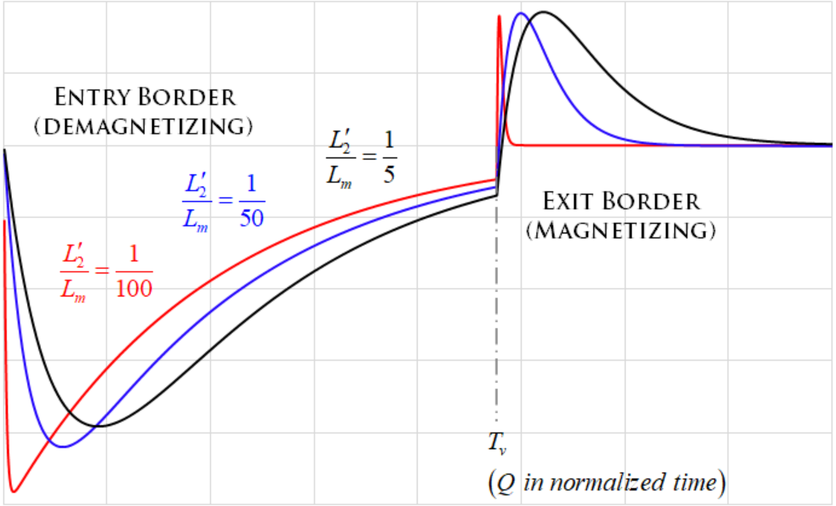

Figure 4. Secondary mmf waves compared, as secondary leakage reactance increases.

The adequate treatment can be given by the transient response of an analog RLC circuit as shown in the Figure 5 (please note that it is not a equivalent circuit!).

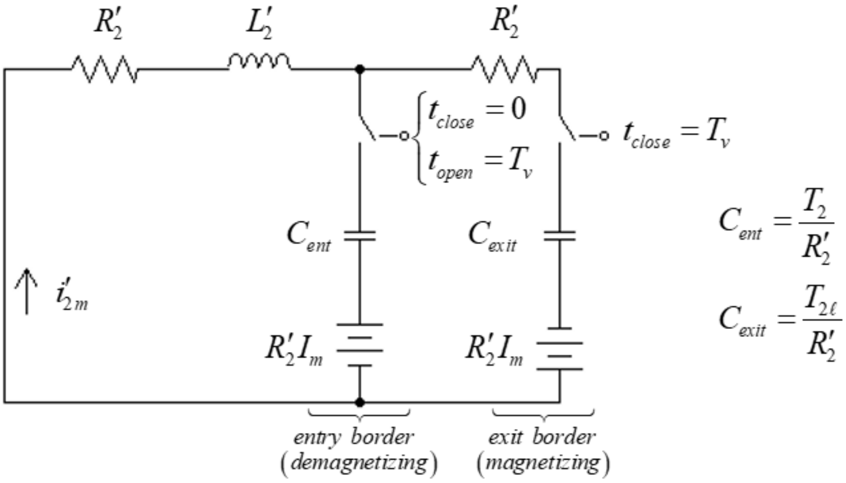

Figure 5. Analogous circuit to describe secondary mmf reaction waves.

The solution to the problem comprises two second-order ordinary differential equations:

$$\frac{d^2 i'_{2m_{ent}}(t)}{dt^2} + \frac{R'_2}{L'_2}\frac{di'_{2m_{ent}}(t)}{dt} + \frac{1}{L'_2 C_{ent}} i'_{2m_{ent}}(t) = 0 \quad (1)$$

$$\frac{d^2 i'_{2m_{exit}}(t)}{dt^2} + \frac{R'_2}{L'_2}\frac{di'_{2m_{exit}}(t)}{dt} + \frac{1}{L'_2 C_{exit}} i'_{2m_{exit}}(t) = 0 \quad (2)$$

Regarding the entry border, the solution will unfold in 3 possible damping cases, which will be considered properly. In applications with relatively large air gaps, it is possible to have a magnetizing inductance smaller than $3L'_2$, what would configure a underdamping case. For the exit border, the case of underdamping is evident, regardless of the values, as will be seen.

These are two series RLC circuits, with different capacitances—one for the entry, the other for exit waves analogy. The analysis of damping for entry border results:

$$\left(\frac{R'_2}{2L'_2}\right)^2 > \frac{1}{L'_2C_{ent}} = \frac{{R'_2}^2}{{L'_2}^2 + L'_2L_m}, \text{if} L_m > 3L'_2 \tag{3}$$

$$\left(\frac{R'_2}{2L'_2}\right)^2 < \frac{1}{L'_2C_{ent}} = \frac{{R'_2}^2}{{L'_2}^2 + L'_2L_m}, \text{if} L_m < 3L'_2 \tag{4}$$

$$\left(\frac{R'_2}{2L'_2}\right)^2 = \frac{1}{L'_2C_{ent}} = \frac{{R'_2}^2}{{L'_2}^2 + L'_2L_m}, \text{if} L_m = 3L'_2 \tag{5}$$

Equations (3)–(5) refer to over (OD), under (UD) and critically damped (CD) situations, respectively. For the exit border, UD is always the case, since:

$$\left(\frac{R'_2}{2L'_2}\right)^2 < \frac{1}{L'_2C_{exit}} = \frac{{R'_2}^2}{{L'_2}^2} \tag{6}$$

Now, applying the general solution for the entry OD, UD and CD transients, considering initial conditions $i'_{2m_{ent}}(0) = 0$ and $v_{C_{ent}}(0) = 0$, that is, $\frac{di'_{2m}(0)}{dt} = -\frac{R'_2 I_m}{L'_2}$, one can have, respectively,

$$i'_{2m_{entOD}}(t) = -\frac{I_m}{k}\sinh\left(\frac{k}{T_{2\ell}}t\right)e^{-\frac{t}{2T_{2\ell}}}, \begin{cases} k = \sqrt{0,25 - T_{2\ell}/T_2} \\ T_{2\ell} = \frac{L'_2}{R'_2}; T_2 = \frac{L'_2 + L_m}{R'_2} \end{cases} \tag{7}$$

$$i'_{2m_{entUD}}(t) = -\frac{I_m}{k'}\sin\left(\frac{k'}{T_{2\ell}}t\right)e^{-\frac{t}{2T_{2\ell}}}, \left\{k' = \sqrt{T_{2\ell}/T_2 - 0,25}\right. \tag{8}$$

$$i'_{2m_{entCD}}(t) = -\frac{I_m}{T_{2\ell}}te^{-\frac{t}{2T_{2\ell}}} \tag{9}$$

In the above solutions, it is easy to see that in the critical damping interface, that is, $L_m = 3L'_2$ and $k = k' = 0$, one have $\lim_{k\to 0} -\frac{I_m}{k}\sinh\left(\frac{k}{T_{2\ell}}t\right)e^{-\frac{t}{2T_{2\ell}}} = \lim_{k'\to 0} -\frac{I_m}{k}\sin\left(\frac{k}{T_{2\ell}}t\right)e^{-\frac{t}{2T_{2\ell}}} = -\frac{I_m}{T_{2\ell}}te^{-\frac{t}{2T_{2\ell}}}$.

If $L'_2 \to 0$, entry wave is always OD, $T_{2\ell} \to 0$ and $k \to 0,5$, and so

$$i'_{2m_{ent}}(t) = \lim_{L'_2\to 0} -\frac{I_m}{k}\sinh\left(\frac{k}{T_{2\ell}}t\right)e^{-\frac{t}{2T_{2\ell}}} = -I_m e^{-\frac{t}{T_2}}$$

$$i'_{2m_{exit}}(t) = \lim_{T_{2\ell}\to 0}\frac{I_m}{T_{2\ell}}(t - T_v)e^{-\frac{t-T_v}{T_{2\ell}}} = 0,$$

which are the expressions obtained by [13].

Then, with respect to the exit transient, the initial conditions are $i'_{2m_{exit}}(T_v+) \approx 0$ and $v_{C_{exit}}(T_v) = 0$, that is, $\frac{di'_{2m_{exit}}(0)}{dt} = \frac{R'_2 I_m}{L'_2}$.

Then, one can obtain

$$i'_{2m_{exit}}(t) = \frac{I_m}{T_{2\ell}}(t - T_v)e^{-\frac{t-T_v}{T_{2\ell}}} \tag{10}$$

Therefore, it is also clear that for $L'_2 \to 0$ there is no consideration of the magnetizing effect on the exit border, as, in fact, is done in [13].

For the current I'_{2m} referred to the primary in phase opposition to the magnetization component I_m, it is sufficient to subtract the exit component from the entry one. From here the absolute value will be considered, for future inclusion in the magnetizing branch of the new model (see Figure 6):

$$I'_{2m} = \frac{1}{T_v}\left[\int_0^{T_v} i'_{2m_{ent}}(t)dt - \lim_{\tau\to\infty}\int_{T_v}^{\tau} i'_{2m_{exit}}(t)dt\right] \tag{11}$$

Considering the dimensionless primary length on normalized time scales $Q = \frac{T_v}{T_2}$ and $Q_\ell = \frac{T_v}{T_{2\ell}}$, the current I'_{2m} results, for entry OD:

$$\begin{aligned} I'_{2mOD} &= I'_{2m_{entOD}} - I'_{2m_{exit}} \\ &= I_m\left[\frac{1}{Q} - \frac{1}{Q_\ell} - e^{-\frac{Q_\ell}{2}}\left(\frac{\sinh(kQ_\ell)}{2Qk} + \frac{\cosh(kQ_\ell)}{Q}\right)\right] \\ &= I_m k_m \end{aligned} \tag{12}$$

For entry UD:

$$\begin{aligned} I'_{2mUD} &= I'_{2m_{entUD}} - I'_{2m_{exit}} \\ &= I_m\left[\frac{1}{Q} - \frac{1}{Q_\ell} - e^{-\frac{Q_\ell}{2}}\left(\frac{\sin(k'Q_\ell)}{2Qk} + \frac{\cos(k'Q_\ell)}{Q}\right)\right] \\ &= I_m k'_m \end{aligned} \tag{13}$$

For entry CD:

$$\begin{aligned} I'_{2mCD} &= I'_{2m_{entCD}} - I'_{2m_{exit}} \\ &= I_m\left[\frac{3}{Q_\ell} - e^{-\frac{Q_\ell}{2}}\left(2 + \frac{4}{Q_\ell}\right)\right] \\ &= I_m k''_m \end{aligned} \tag{14}$$

One can see the new magnetizing reactance in Figure 6, where the correction factor can be k_m, k'_m or k''_m, according to the entry transient damping.

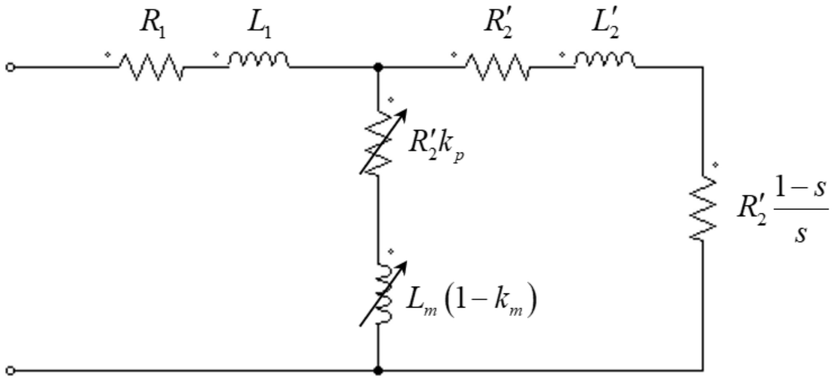

Figure 6. New proposed equivalent circuit considering all secondary leakage effects.

Next, eddy losses must be corrected due to the path taken by the secondary reaction currents. First, one have to consider entry and exit waves components:

$$R'_2\left[\sqrt{\frac{1}{T_v}\left[\int_0^{T_v} {i'_{2m_{ent}}}^2(t)dt + \lim_{\tau\to\infty}\int_{T_v}^{\tau} {i'_{2m_{exit}}}^2(t)dt\right]}\right]^2 \tag{15}$$

Secondly, the component corresponding to the stored energy that dissipates at exit border must be taken into account, considering the value of magnetizing current at this edge:

$$\begin{aligned}&\tfrac{1}{2}(L_m+L'_2)[I_m+i'_{m2_{ent}}(T_v)]^2\tfrac{1}{T_v}=\\&=\tfrac{1}{2}(L_m+L'_2)[I_m+i'_{m2_{ent}}(T_v)]^2\tfrac{R'_2}{(L_m+L'_2)Q}\\&=\tfrac{R'_2}{2Q}[I_m+i'_{m2_{ent}}(T_v)]^2\end{aligned}\tag{16}$$

Again, for entry OD, summing up the cited effects:

$$\begin{aligned}&R'_2I_m^2\left[\frac{1}{Q}+\frac{1}{4Q_\ell}-e^{-Q_\ell}\left(\frac{1}{2Q}+\frac{\sinh(2kQ_\ell)}{4kQ}+\right.\right.\\&\left.\left.+\frac{4e^{\frac{Q_\ell}{2}}\sinh(kQ_\ell)}{4kQ}-\frac{\sinh^2(kQ_\ell)}{4k^2Q}\right)\right]\\&=R'_2k_pI_m^2\end{aligned}\tag{17}$$

For entry UD:

$$\begin{aligned}&R'_2I_m^2\left[\frac{1}{Q}+\frac{1}{4Q_\ell}-e^{-Q_\ell}\left(\frac{1}{2Q}+\frac{\sin(2k'Q_\ell)}{4k'Q}+\right.\right.\\&\left.\left.+\frac{4e^{\frac{Q_\ell}{2}}\sin(k'Q_\ell)}{4k'Q}-\frac{\sin^2(k'Q_\ell)}{4k'^2Q}\right)\right]\\&=R'_2k'_pI_m^2\end{aligned}\tag{18}$$

For entry CD:

$$\begin{aligned}&R'_2I_m^2\left[\frac{1}{2Q}+\frac{9}{4Q_\ell}-e^{-Q_\ell}\left(Q_\ell+2+\right.\right.\\&\left.\left.+\frac{2}{Q_\ell}+\frac{Q_\ell}{2Q}\left(2e^{\frac{Q_\ell}{2}}-Q_\ell\right)\right)\right]\\&=R'_2k''_pI_m^2\end{aligned}\tag{19}$$

Similarly, in Figure 6 one can calculate the eddy losses with correction factors k_p, k'_p or k''_p.

2.2. Tranverse Edge Effects

For solid secondaries with a width greater than the primary, there is the simplified Russell and Norsworthy factor for the ν^{th} harmonic, modified by [8]:

$$k_{RN_\nu}=1-\frac{\tanh\left(\nu\frac{\pi\ell_{z2}}{2\tau_p}\right)}{\nu\frac{\pi\ell_{z2}}{2\tau_p}\left[1+\left(1+1.3\frac{t_{ov}-d}{d}\right)\tanh\left(\nu\frac{\pi\ell_{z2}}{2\tau_p}\right)\tanh\left(\nu\frac{\pi h_{ov}}{\tau_p}\right)\right]}\tag{20}$$

The main difference from the slotted secondary, as far as transverse effects are concerned, is that there is no lateral extension of a conductive plate, but of the cage bars.

Equation (20) is for solid secondaries. Considering the adaptations of Figure 7, it can be used in the case of slotted ones.

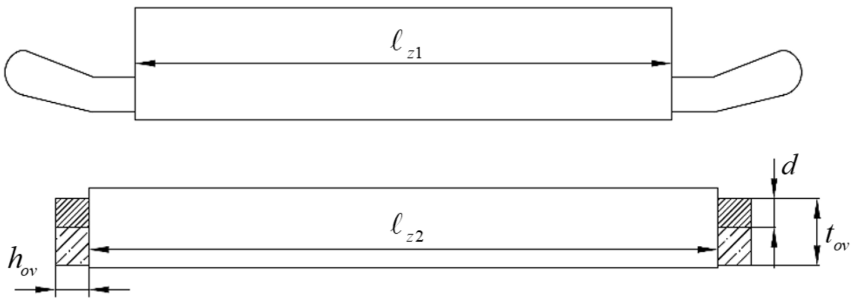

Figure 7. Section view of linear motor with slotted secondary.

2.3. Half-Filled Slots

The end slots of the primary core, in double-layer windings, inevitably become half-filled, as shown in Figure 8. The distribution of primary magnetomotive forces is affected and, consequently, the magnetizing branch and secondary parameters referred to the primary as well [19].

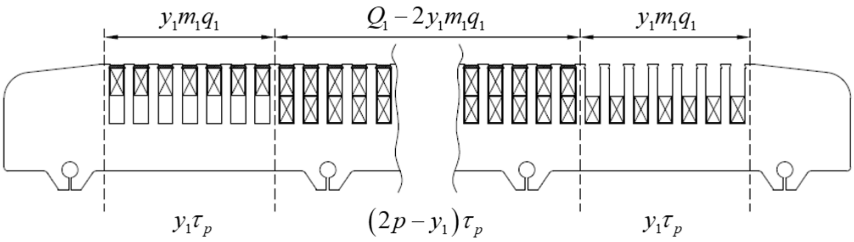

Figure 8. Slot number and lengths with half-filled slots, according to [19].

The primary mmf distribution is approximately halved in the two sections where the slots are partially filled, so the number of slots and the equivalent length can be calculated as

$$Q'_1 = Q_1 - 2y_1 m_1 q_1 + y_1 m_1 q_1 = Q_1 - y_1 m_1 q_1 \tag{21}$$

$$D' = (2p - y_1)\tau_p + y_1 \tau_p = 2p\tau_p = Q'_1 \tau_{s1} \tag{22}$$

2.4. Vertical Forces

Applying the new approach to the vertical attractive forces, the RMS value of the effective magnetization current is calculated, keeping in mind the existing proportionality in the main portion in relation to the stored energy:

$$F_{v_{att}} = \frac{3}{2\ell_g} L_m \left[\sqrt{\frac{1}{T_v} \left[\int_0^{T_v} \left(I_m + i'_{2m_{ent}}(t)\right)^2 dt + \lim_{\tau \to \infty} \int_{T_v}^{\tau} {i'_{2m_{exit}}}^2(t) dt \right]} \right]^2 \tag{23}$$

Again, for entry OD:

$$\begin{aligned} F_{v_{attOD}} &= \tfrac{3}{2\ell_g} L_m I_m^2 \Big[1 + \tfrac{1}{4Q_\ell} - \tfrac{3}{2Q} - \\ &- e^{-Q_\ell} \Big[\tfrac{1}{2Q} + \tfrac{\sinh(2kQ_\ell)}{4kQ} + \tfrac{\cosh(2kQ_\ell) - 1}{8k^2 Q} - \\ &- e^{\frac{Q_\ell}{2}} \left(\tfrac{\sinh(kQ_\ell)}{kQ} + \tfrac{2\cosh(kQ_\ell)}{Q} \right) \Big] \Big] \\ &= \tfrac{3}{2\ell_g} k_v L_m I_m^2 \end{aligned} \tag{24}$$

For entry UD:

$$\begin{aligned} F_{v_{attUD}} &= \tfrac{3}{2\ell_g} L_m I_m^2 \Big[1 + \tfrac{1}{4Q_\ell} - \tfrac{3}{2Q} - \\ &- e^{-Q_\ell} \Big[\tfrac{1}{2Q} + \tfrac{\sin(2k'Q_\ell)}{4k'Q} - \tfrac{\cos(2k'Q_\ell) - 1}{8k'^2 Q} - \\ &- e^{\frac{Q_\ell}{2}} \left(\tfrac{\sin(k'Q_\ell)}{k'Q} + \tfrac{2\cos(k'Q_\ell)}{Q} \right) \Big] \Big] \\ &= \tfrac{3}{2\ell_g} k'_v L_m I_m^2 \end{aligned} \tag{25}$$

For entry CD:

$$\begin{aligned} F_{v_{atrCD}} &= \frac{3}{2\ell_g} L_m I_m^2 \left[1 + \frac{1}{4Q_\ell} - \frac{6}{Q_\ell} + \right. \\ &\left. + 4e^{-\frac{Q_\ell}{2}} \left(1 + \frac{2}{Q_\ell}\right) - e^{-Q_\ell}\left(Q_\ell + 2 + \frac{2}{Q_\ell}\right)\right] \\ &= \frac{3}{2\ell_g} k''_v L_m I_m^2 \end{aligned} \tag{26}$$

As for the repulsion component, the expression according to [13] remains:

$$F_{v_{rep}} = k_r \frac{{I'_2}^2}{h_{12}} \tag{27}$$

The length h_{12} now corresponds to the distance between the centers of the primary and secondary conductors. The constant k_r must be determined from static tests. The results for this constant are shown in the next section.

3. Experimental Tests and Discussion

The manufacturing of a linear motor for tests involves certain difficulties, mainly with regard to the measurement of traction and vertical forces. In the case of the present work, a round geometry was chosen, as will be shown next.

3.1. Prototype

In order to expand the possibilities of experimental data, a double secondary was built: slotted and solid. The short primary was made in such a way as to be able to move laterally, sometimes coupling with the slotted secondary, sometimes with the solid. Part of the design can be viewed in Figure 9. The solid secondary will be treated with more closely attention in a future work. For the purposes of this present article, the efforts are concentrated in the slloted one.

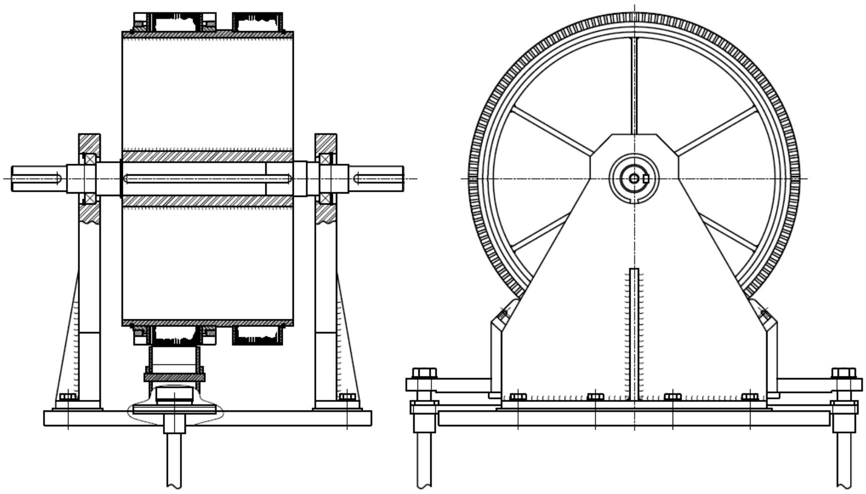

Figure 9. Prototype design.

In addition, vertical axes on the sides, guided by lateral bearings, made it possible to measure vertical forces.

The machine was conceived and built in the facilities of Equacional Elétrica e Mecânica company, where the photographs found in Figures 10 and 11 were taken.

Figure 10. Prototype on test bench.

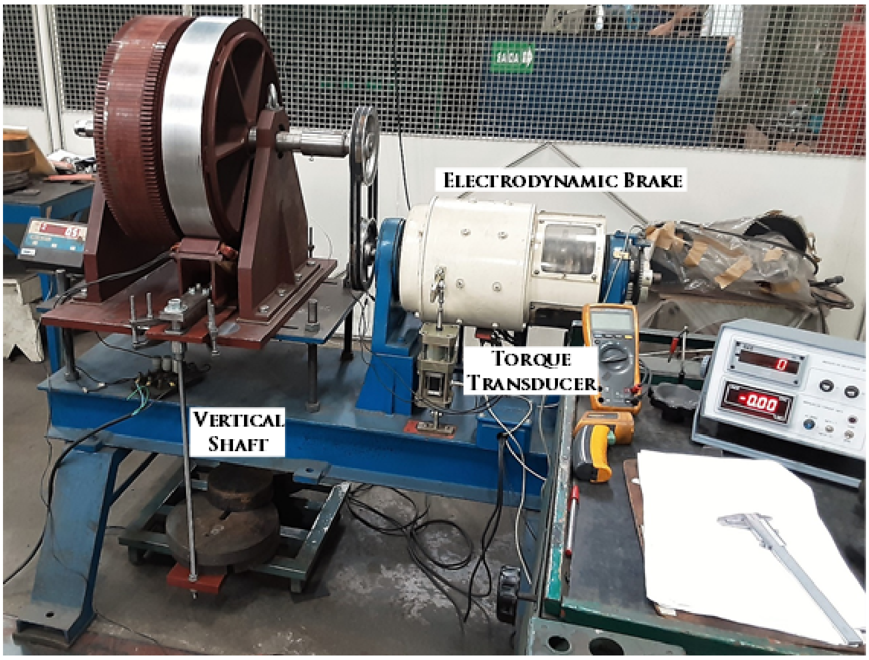

Figure 11. Test bench main items.

The concentricity of the primary and secondary radii occurs with an air gap equal to 2 mm (5 mm in the case of the solid secondary, considering the thickness of the conductive sheet). Any value other than this results in different air gaps across the primary. Thus, mean values at the experimental points were considered.

In Table 1, one can see the rated and constructive data of the prototype. For the purposes of this paper, only the slotted secondary was considered and tested. The comparison with the solid one will be presented in a future work.

Table 1. Rated values of the prototype.

Data	Value	Data	Value
v [m/s]	2.6–13.5	P_{thr}[kW]	0.3–2.4
F_{thr} [N]	120–175	$V_{1_{line}}$[V]	87.5–437.5
f [Hz]	30–150	$2p$	8
m_1	3	N_1	256
l_{z1} [mm]	80	l_{z2}[mm]	90
Q_1/Q_1'	26/24	Q_2/Q_2'	38/35

The parameters of the equivalent circuit, in a airgap range of 1.86–4.24 mm, are shown in Table 2. The values do not comprise heat and skin effect corrections—these were conveniently taken into account according to frequency and temperature measured in tests.

Table 2. Calculated parameters for the prototype.

Parameter	Value	Parameter	Value
l_g [mm]	1.86–4.24	k_{RN}	0.844
R_1 [Ω/ph]	0.646	R_2' [Ω/ph]	0.524
L_1 [mH/ph]	7.58–7.36	L_2' [mH/ph]	4.31–4.20
L_m [mH/ph]	18.1–8.54	L_m/L_2'	4.2–2.0

One can see that the air-gap range demands different treatments for the entry wave (OD, UD, and CD, eventually).

3.2. Curves Compared

The prototype was tested in order to compare different conditions of source frequency and air-gap length. The test bench is shown in Figures 10 and 11.

The thrust force was measured through a torque transducer in the electrodynamic brake, considering its lever arm length and the secondary diameter. The vertical force, on the other hand, was measured by difference of mass in a calibrated scale. The prototype had two vertical shafts through linear bearings, in order to eliminate undesirable frictions.

In Figure 12, one can see the source frequency influence on thrust force, along with the experimental points. The other curves ("No Correction", that is, the classic induction motor equivalent circuit; and "Duncan") serve the purpose of analysis for the new model precision and contribution. Here, the air gaps in the prototype are according to entry OD cases.

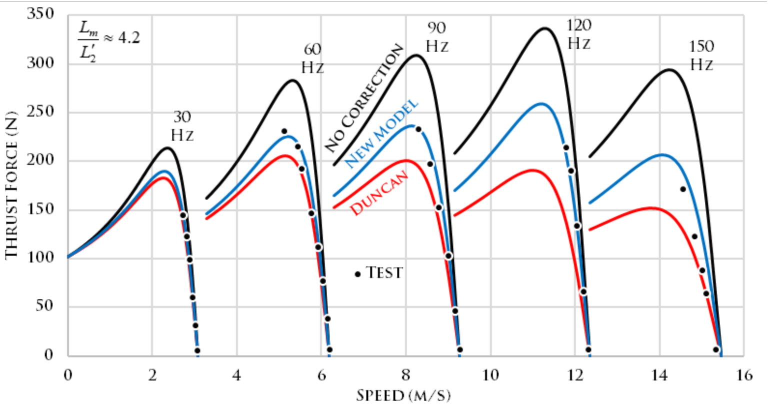

Figure 12. Comparison of thrust force through frequency variation (OD). Average gaps in ascending order [mm]: 1.86/2.15/2.21/2.32/2.35.

In sequence, Figure 13 shows, with the same average gaps, the behavior of resulting vertical forces through frequency variation. The dots, once more, are experimental points.

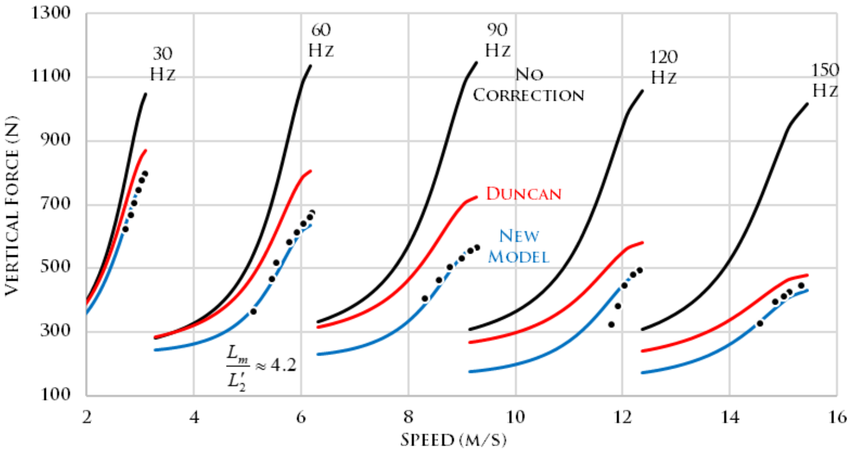

Figure 13. Comparison of vertical force through frequency variation (OD). Average gaps in ascending order [mm]: 1.86/2.15/2.21/2.32/2.35.

For the determination of constant k_r, the locked secondary tests were necessary. Frequencies from 30 to 150 Hz, with average gaps from 1.86 to 4.24 mm, resulted in values presented in Table 3. It has been observed that not just the air gap and the frequency, but the damping case (OD or UD) has influence on this factor.

Table 3. Experimental k_r values for various frequencies and average air gaps.

mm/Hz	1.86/30	2.15/60	2.21/90	2.32/120	2.35/150
k_r	0.00637	0.00487	0.00337	0.00330	0.00330
mm/Hz	3.89/30	3.99/60	4.11/90	4.23/120	4.24/150
k_r	0.0160	0.0155	0.0155	0.0120	0.0130

The different values of average air gaps need some clarification, and this has to do with difficulties faced during experimental tests. First, values are average because the prototype is round, resulting in eccentric radii for most cases. Second, with the variation of measured vertical forces along the tests, changes in air gap have occurred, since the method of measurement involves vertical displacement. In the prototype design, the primary remains supported on the scale by means of vertical axes and linear bearings. In this way, the different vertical forces along the tests provide different bending in the longer pieces, changing a little bit the distance between primary and secondary. This is a weakness of the prototype, to be mitigated in further studies.

Another difficulty in the experiments was the temperature of primary and specially of secondary windings, because of its great effect on the thrust force shape. Some adapted ventilation system was used so that the measurements took place with approximately the same temperatures in such windings. In the extreme cases, corrections were made to a reference temperature. Be means of a thermographic camera, the secondary temperature could be measured.

In the same way of Figures 12 and 13 (entry overdamped case), thrust and vertical forces are also presented for higher values of air gap in Figures 14 and 15—this time, according to entry underdamped cases.

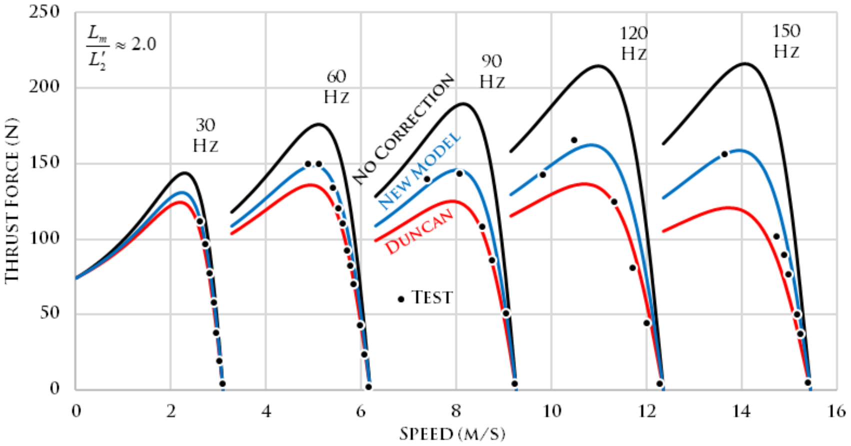

Figure 14. Comparison of thrust force through frequency variation (UD). Average gaps in ascending order [mm]: 3.89/3.99/4.11/4.23/4.24.

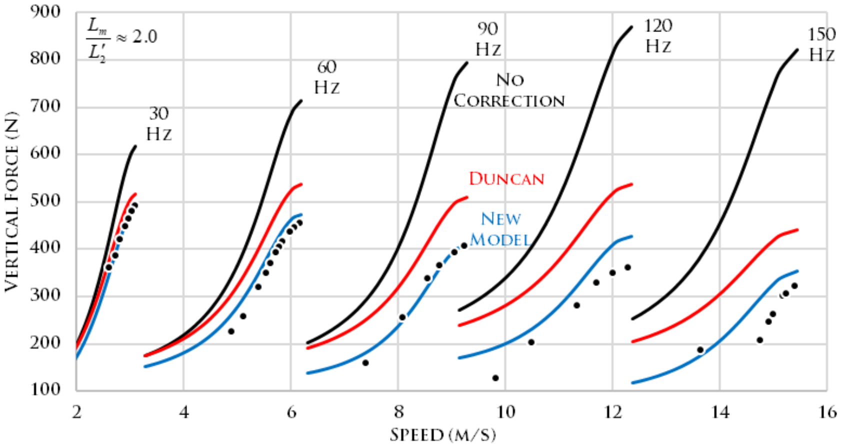

Figure 15. Comparison of vertical force through frequency variation (UD). Average gaps in ascending order [mm]: 3.89/3.99/4.11/4.23/4.24.

4. Conclusions

The proposed model have shown reasonable accuracy in thrust and vertical forces prevision. The proposed circuit proved to be useful in cases where the secondary leakage inductance is not negligible.

As the frequency increases, the time required to travel the effective length of the primary will decrease, accentuating the demagnetizing (entry) and magnetizing (exit) effects. However, at the same time, increasing the frequency will also accentuate the skin effect, so as to increase the secondary resistance and decrease the secondary leakage. Depending on the case, there will be a range of frequencies where the model will be much more accurate than [13].

The relevance of the secondary leakage reactance, in the authors calculations, was more substantially present in its influence through the rise of the demagnetizing entry wave.

Finally, the work paves the way for some future paths, such as the optimization of the prototype regarding the measurement of vertical force with constant air gap, better development of a method for determine the equivalent circuit from tests and application of the model to other types of linear induction motors, such as double primary and/or secondary without back iron.

Author Contributions: Conceptualization, D.R.G.; methodology, D.R.G.; validation, D.G and I.E.C.; formal analysis, D.R.G. and I.E.C.; investigation, D.R.G.; resources, D.R.G.; data curation, D.R.G.; writing—original draft preparation, D.R.G.; writing—review and editing, D.R.G. and I.E.C.; supervision, I.E.C. All authors have read and agreed to the published version of the manuscript.

Funding: This research received no external funding by institutions with grant number.

Data Availability Statement: Not applicable.

Acknowledgments: The manufacture of the prototype, as well as space and machinery for testing were donated and/or provided by the company Equacional Elétrica e Mecânica.

Conflicts of Interest: The authors declare no conflict of interest.

References

1. Laithwaite, E.R.; Barwell, F.T. Application of Linear Induction Motors to High-speed Transport Systems. *Proc. Inst. Electr. Eng.* **1969**, *116*, 713–724. [CrossRef]
2. Alscher, H.; Boldea, I.F.; Eastham, A.R.; Iguchi, M. Propelling Passengers Faster Than a Speeding Bullet: As Maglev Urban Railways Get Tracking, Lines in West Germany, Japan, and Canada Are Expected to Follow England's Commercial Lead. *IEE Spectr.* **1984**, *21*, 57–64. [CrossRef]
3. Laithwaite, E.R. Linear Induction Motors. *Proc. IEE Part A Power Eng.* **1957**, *104*, 461–470. [CrossRef]
4. Nasar, S.A. Electromagnetic Fields and Forces in a Linear Induction Motor, Taking Into Account Edge Effects. *Proc. Inst. Electr. Eng.* **1969**, *116*, 605–608. [CrossRef]
5. Laithwaite, E.R. Some Aspects of Electrical Machines With Open Magnetic Circuits. *Proc. Inst. Electr. Eng.* **1968**, *115*, 1275–1283. [CrossRef]
6. Yamamura, S.; Ito, H.; Ishulawa, Y. Theories of the Linear, Induction Motor and Compensated Linear Induction Motor. *IEEE Trans. Power Appar. Syst.* **1972**, *PAS-91*, 1700–1710. [CrossRef]
7. Lee, C.H.; Chin, C.Y. A Theoretical Analysis of Linear Induction Motors. *IEEE Trans. Power Appar. Syst.* **1979**, *PAS-98*, 679–688. [CrossRef]
8. Gieras, J.F.; Dawson, G.E.; Eastham, A.R. A New Longitudinal End Effect Factor for Linear Induction Motors. *IEEE Trans. Energy Convers.* **1987**, *EC-2*, 152–159. [CrossRef]
9. Pai, R.M.; Boldea, I.; Nasar, S.A. A Complete Equivalent Circuit of a Linear Induction Motor With Sheet Secondary. *IEEE Trans. Magn.* **1988**, *24*, 639–654. [CrossRef]
10. Zhang, Z.; Eastham, T.R.; Dawson, G.E. LIM Dynamic Performance Assessment from Parameter Identification. In Proceedings of the Conference Record of the 1993 IEEE Industry Applications Conference Twenty-Eighth IAS Annual Meeting, Toronto, ON, Canada, 2–8 October 1993.
11. Hofmann, R.; Binder, A.; Pfeiffer, R. Investigations on a Linear Induction Machine for Railway Applications. In Proceedings of the IEEE International Electric Machines and Drives Conference, Cambridge, MA, USA, 17–20 June 2001.
12. Woronowicz, K.; Safaee, A. A Novel Linear Induction Motor Equivalent-Circuit With Optimized End Effect Model. *Can. J. Electr. Comput. Eng.* **2014**, *37*, 34–41. [CrossRef]
13. Duncan, J. Linear Induction Motor–Equivalent Circuit Model. *IEE Proc. B–Electr. Power Appl.* **1983**, *130*, 51–57. [CrossRef]
14. Koseki, T.; Sone, S.; Yokoi, T.; Ebihara, D.; Osawa, S. Investigation on Secondary Slot Pitches of a Cage-type Linear Induction Motor. *IEEE Trans. Magn.* **1993**, *29*, 2944–2946. [CrossRef]
15. Park, S.C.; Kim, B.T. Effect of Contact Resistance Between Side-bar and Secondary Conductors in a Linear Induction Motor With a Cage-type Secondary. *IEEE Trans. Magn.* **2003**, *39*, 1562–1565. [CrossRef]
16. Ravanji, M.H.; Nasiri-Gheidari, Z. Design Optimization of a Ladder Secondary Single-Sided Linear Induction Motor for Improved Performance. *IEEE Trans. Energy Convers.* **2015**, *30*, 1595–1603. [CrossRef]
17. Koseki, T.; Sone, S.; Yokoi, T.; Ebihara, D. Analysis of secondary eddy current path of a linear induction motor. In *Proceedings of Linear Drive Symposium*; LD-92-100; IEEE: Tokyo, Japan, 1992; pp. 21–29.
18. Yamaguchi, T.; Ito, M.; Matsui, K. Improvement of thrust of linear induction motor using modified ladder slits. In Proceedings of the Power Conversion Conference—-PCC'97, Nagaoka, Japan, 6 August 1997; Volume 2, pp. 563–566
19. Lv, G.; Zhou, T.; Zeng, D. Design of Ladder-Slit Secondaries and Performance Improvement of Linear Induction Motors for Urban Rail Transit. *IEEE Trans. Ind. Electron.* **2018**, *65*, 1187–1195. [CrossRef]
20. Xu, W.; Zhu, J.G.; Zhang, Y.; Li, Y.; Wang, Y.; Guo, Y. An Improved Equivalent Circuit Model of a Single-Sided Linear Induction Motor. *IEEE Trans. Veh. Technol.* **2010**, *59*, 2277–2289. [CrossRef]
21. Zare-Bazghaleh, A.; Meshkatoddini, M.Z.; Fallah-Choolabi, E. Derivation of Equivalent Circuit Parameters for Single-Sided Linear Induction Motors. *Plasma Sci. IEEE Trans.* **2015**, *44*, 3637–3644. [CrossRef]
22. Lv, G.; Zeng, D.; Zhou, T.; Degano, M. A Complete Equivalent Circuit for Linear Induction Motors With Laterally Asymmetric Secondary for Urban Railway Transit. *IEEE Trans. Energy Convers.* **2021**, *36*, 1014–1022. [CrossRef]

23. Hirahara, H.; Inoue, M.; Yamamoto, S. A Method for Determining Equivalent Circuit Constant of Linear Induction Motors Using Locked Mover and Standstill Impedance Tests. In Proceedings of the IEEE International Power Electronics Conference, Himeji, Japan, 15–19 May 2022.
24. Heidari, H.; RassÕLKIN, A.; Razzaghi, A.; Vaimann, T.; Kallaste, A.; Andriushchenko, E.; Belahcen, A.; Lukichev, D.V. A Modified Dynamic Model of Single-Sided Linear Induction Motors Considering Longitudinal and Transversal Effects. *Electronics* **2021**, *10*, 933. [CrossRef]
25. Lv, G.; Zeng, D.; Zhou, T. An Equivalent Circuit of the Single-Sided Linear Induction Motor Considering the Discontinuous Secondary. *IET Electr. Power Appl.* **2019**, *13*, 31–37. [CrossRef]
26. Teriaiev, V.; Dovbyk, A.; Kornienko, V.; Pechenik, M.; Buryan, S. Generalized Mathematical Model of a Linear Induction Motor. In Proceedings of the 2022 IEEE 41st International Conference on Electronics and Nanotechnology (ELNANO), Kyiv, Ukraine, 10–14 October 2022; pp. 741–745. [CrossRef]
27. Di J.; Fletcher, J.E.; Fan, Y.; Liu, Y.; Sun, Z. Design and Performance Investigation of the Double-Sided Linear Induction Motor With a Ladder-Slot Secondary. *IEEE Trans. Energy Convers.* **2019**, *34*, 1603–1612. [CrossRef]
28. Zhang, L.; Obeid, H.; Laghrouche, S.; Cirrincione, M. Second Order Sliding Mode Observer of Linear Induction Motor. *IET Electr. Power Appl.* **2019**, *13*, 38–47. [CrossRef]
29. Sotelo, G.G.; de Andrade, R., Jr.; Dias, D.H.N.; Ferreira, A.C.; Costa, F.; Machado, O.J.; de Oliveira, R.A.H.; Santos, M.D.A.; Stephan, R.M. Tests with One Module of the Brazilian Maglev-Cobra Vehicle. *IEEE Trans. Appl. Supercond.* **2013**, *23*, 3601204. [CrossRef]
30. Mattos, L.S.; Rodriguez, E.; Costa, F.; Sotelo, G.G.; de Andrade, R., Jr.; Stephan, R.M. MagLev-Cobra Operational Tests. *IEEE Trans. Appl. Supercond.* **2016**, *26*, 3600704. [CrossRef]